Materials Horizons

Accepted Manuscript

This article can be cited before page numbers have been issued, to do this please use: W. Shi, M. Mo, Q. Hu, L. Xu, S. Guan, Z. Tan, J. Xing and Q. Chen, *Mater. Horiz.*, 2025, DOI: 10.1039/D5MH01252J.




ROYAL SOCIETY OF CHEMISTRY

rsc.li/materials-horizons

View Article Online
DOI: 10.1039/D5MH01252J

# New Concepts

$CaBi_2Ta_2O_9$ (CBTa) is a typical two layered bismuth layered ferroelectrics (BLSFs) compound with a high $T_C$ value of 923 ºC. However, its application is hindered by a low piezoelectric coefficient $d_{33}$, and conventional doping strategies have offered limited improvement. In this work, we report a thermal-activated grain plastic rearrangement strategy that enables the fabrication of [100]-textured CBTa based ceramics without the use of any templates.

By integrating crystallographic phenomenological theory with first-principle calculations, we demonstrate that the [100]-textured ceramics can achieve a $d_{33}$ enhancement of 68% compared to pure CBTa ceramics. Using the proposed grain plastic rearrangement method, we successfully fabricated [100]-textured CNBT-LC ceramics. Specifically, an ultra-high $d_{33}$ value of 21.8 pC/N with excellent thermal stability (only a 5% decrease compared to the initial value after depoling at 900 ºC for 2 h) is obtained in textured CNBT-LC ceramics. Moreover, the direct-current (*dc*) resistivity ($\rho$) of textured CNBT-LC ceramics has been significantly improved. At 600 °C, the resistivity of textured ceramics is more than $1.11\times10^7$ Ω·cm, while that of traditionally sintered ceramics with random orientation only remains $1.92\times10^6$. It is worth noting that the $d_{33}$ values and *dc* resistivity (at 600 ºC) of textured CNBT-LC ceramics in this work are superior compared with other reported typical two-layered BLSFs systems.

This study establishes a broadly applicable and straightforward strategy for inducing texture in heavily doped BLSFs, highlighting the role of grain plastic rearrangement and domain growth kinetics in enhancing their electrical properties.

View Article Online
DOI: 10.1039/D5MH01252J

## Data Availability Statement

The data that support the findings of this study are available from the corresponding author upon reasonable request.

View Article Online
DOI: 10.1039/D5MH01252J

# Inducing superior electrical performances in textured $CaBi_2Ta_2O_9$ based ceramics

Wei Shi, Mingyue Mo, Qi Hu, Zhi Tan, Shangyi Guan, Liang Xu, Jie Xing, Qiang Chen*

College of Materials Science and Engineering, Sichuan University, Chengdu, China

*Corresponding author: Qiang Chen; E-mail address: cqscu@scu.edu.cn





## Abstract

Bismuth-layered structure ferroelectrics (BLSFs), exemplified by $CaBi_2Ta_2O_9$ (CBTa), exhibit exceptional thermal stability at high temperatures with high Curie temperature. This attribute renders them highly promising candidates for piezoelectric sensors, transducers, and non-volatile ferroelectric memory, etc. working in extreme environments. However, CBTa ceramic suffers from intrinsic limitations: spontaneous polarization confined within the *ab*-plane of the unit cell and a large coercive field, leading to severely suppressed piezoelectric activity ($d_{33} \approx 5.4$ pC/N). To address these challenges, a synergistic strategy integrating ion doping and hot forging is proposed to fabricate textured CBTa-based ceramics. Systematic characterizations reveal that the hot forging induces preferential grain orientation, effectively aligning polar domains while maintaining the layered perovskite structure. This optimization achieves significant enhancement in piezoelectric response ($d_{33}$~21.8 pC/N) and direct-current resistivity ($\rho$>1×10$^7$ Ω·cm at 600 °C) without compromising $T_C$ (~922 °C). Notably, the textured ceramics remain 95% of their initial piezoelectric performance after depoling at 900 °C for 2 h, underscoring their outstanding thermal stability. This work establishes a microstructure-engineering paradigm for tailoring electromechanical properties in BLSFs, bridging the gap between intrinsic material limitations and application-driven performance requirements.

**Keywords**: $CaBi_2Ta_2O_9$, hot forging, textured ceramics, first-principle calculation, piezoelectric properties

View Article Online
DOI: 10.1039/D5MH01252J





## 1. Introduction

Piezoelectric materials, which exhibit the ability to interconvert mechanical and electrical energy through the piezoelectric effect, have been extensively utilized in ultrasonic transducers, piezoelectric sensors, vibration sensors, and various other advanced applications[1-7]. The continuous demand for high-performance piezoelectric materials is crucial for the advancement of modern science and technology, driving research efforts toward enhancing their functional properties and expanding their applicability[8]. Among the widely studied piezoelectric materials, $ABO_3$-type ceramics with perovskite structure have garnered significant attention due to their excellent electromechanical performances[9-13]. Lead-based perovskite ceramics, such as Pb(Zr, Ti)$O_3$ (PZT) ceramics, exhibit outstanding piezoelectric coefficients and electromechanical coupling coefficients[14, 15]. However, their environmental toxicity and stringent regulations on lead usage pose significant challenges for their sustainable application. Meanwhile, other lead-free alternatives, such as $K_{0.5}Na_{0.5}NbO_3$ (KNN) based ceramics, have demonstrated promising piezoelectric properties, yet their poor stability and reproducibility severely limit their practical implementation[16]. More critically, a common drawback shared by both lead-based and lead-free perovskite ceramics is their relatively low Curie temperature ($T_C$<400 °C, rendering them unsuitable for extreme environments where high-temperature piezoelectric sensors must be operated at 500 °C or above, such as in aerospace, nuclear energy systems, and harsh industrial settings[17]. In contrast, bismuth-layered structure ferroelectrics (BLSFs) have emerged as one of the most promising candidates for high-temperature piezoelectric sensors due to their intrinsically high $T_C$, excellent thermal stability, and low aging rates[16, 18]. These favorable properties make BLSFs particularly attractive for long-term operation in extreme environments[19]. Disappointingly, their practical application is hindered by their inherently low piezoelectric coefficients ($d_{33}$<5 pC/N), which fail to meet the sensitivity requirements of high-performance sensors[20-22]. Consequently, enhancing the piezoelectric properties of BLSFs without compromising their $T_C$ remains a major challenge in this system and addressing this issue is essential for unlocking their full potential in next-generation high-temperature piezoelectric devices.

Among the members of the BLSFs family, $CaBi_2Ta_2O_9$ (CBTa) and $CaBi_2Nb_2O_9$ (CBN) ceramics are the typical two-layered Aurivillius type compounds, both exhibiting a similar $T_C$ of approximately 925 °C[23]. However, despite this similarity,

CBTa-based ceramics stand out due to their exceptional high-temperature resistivity ($\rho$~$10^6$ Ω·cm at 600 °C, which is significantly higher than that of CBN-based ceramics (ρ~$10^5$ Ω·cm at 600 °C[24, 25]. The outstanding electrical resistivity and excellent anti-aging characteristics make CBTa based ceramics a highly valuable candidate for high-temperature applications. Nevertheless, its practical utilization remains limited due to its inherently low piezoelectric coefficient ($d_{33}$ < 5 pC/N) and large coercive field, posing significant challenges for its application in highly sensitive piezoelectric devices. In recent years, chemical doping has been explored as an effective strategy to enhance the piezoelectric properties of CBTa ceramics[16]. For instance, ($Li_{0.5}Pr_{0.5}$) co-substitution at A-site has been reported to increase the $d_{33}$ value to 15.1 pC/N at doping concentration of 4%, representing a threefold improvement over undoped CBTa ceramics[26]. Additionally, Wu et al. developed a novel Aurivillius solid solution by incorporating $Na_{0.5}Bi_{2.5}Ta_2O_9$ (NBT) into CBTa through conventional sintering process, achieving a gradual enhancement in piezoelectricity ($d_{33}$~12.8 pC/N) while maintaining excellent temperature stability, with $d_{33}$ retaining 94% of its initial value after annealing at 900 °C[27]. Similarly, Chen et al. introduced a CBN-based component into CBTa ceramics, resulting in a solid solution with significantly improved comprehensive properties ($d_{33}$ ~ 14.1 pC/N, $\rho$ ~ $1.08\times10^6$ Ω·cm at 600 °C [23]. Although these studies have demonstrated that chemical doping can effectively enhance the piezoelectric performances of CBTa ceramics, the improvements remain limitation, and achieving a $d_{33}$ value exceeding 20 pC/N becomes a significant challenge. Furthermore, doping induced modifications often come at the cost of reduced $T_C$, which compromises the material's high-temperature stability.

Meanwhile, considering the strong anisotropic features for the crystal structure of CBTa and the fact that texturing techniques proved to be extremely effective as a modification strategy in BLSFs other than CBTa based ceramics, this study explores an alternative approach of hot forging to achieve controlled texturing and optimize chemically doped CBTa ceramics. This technique not only significantly enhances piezoelectric properties but also preserves high $T_C$, thereby offering a promising pathway for the development of high-performance, high-temperature piezoelectric materials.

## 2. Results and discussion

BLSFs, including CBTa, exhibit pronounced anisotropy due to their distinctive layered structure, as illustrated in Figure 1a. The dependence of piezoelectric constants

on crystallographic orientation can be addressed through tensor transformation. In general, the space group of two-layered BLSFs compounds (such as CBN, CBTa, NBN, etc.) reported in the literature is represented as $A2_1am$.[17, 25, 45] However, since the spontaneous polarization vector ($P_s$) of the $Cmc2_1$ space group is naturally aligned with the *c*-axis of the Cartesian coordinate system, this eliminates the need for complex coordinate axis transformations (such as swapping *a*-axis ↔ *c*-axis) required in the $A2_1am$ space group. Selecting $Cmc2_1$ space group significantly simplifies the calculation process for orientation-dependent piezoelectric coefficients (such as $d_{33}$) in textured ceramics while ensuring the accuracy of the physical description and computational efficiency. Initially, the piezoelectric tensor $d_{ijk}^0$ of CBTa ferroelectrics with $Cmc2_1$ space group is calculated from the original coordinate systems $x_1^0$, $x_2^0$ and $x_3^0$ along the [100], [010] and [001] direction. It is clear that only 5 independent components are not zero, namely $d_{31}^0$, $d_{32}^0$, $d_{33}^0$, $d_{24}^0$, and $d_{15}^0$. When stress acts on CBTa ceramics in a direction different from that of the original coordinate axes, the new coefficient $d'_{ijk}$ can be deduced from $d_{ijk}^0$ through tensor transformation, which depends on the relationship between new and primitive coordinate systems, as follows:

$$d'_{ijk} = a_{im}a_{jn}a_{kp}d^0_{mnp} \quad (1)$$

where $a_{ij}$ represents the elements of transformation matrix and defined as the cosines of angles between the original axis $x_i^0$ in the Cartesian coordinate system $\{x_1^0,\ x_2^0,\ x_3^0\}$ and the new axis $x'_j$ in $\{x'_1,\ x'_2,\ x'_3\}$, and the Einstein summation is applied. It is worth noting that conventional sintered ceramics consist of numerous grains with random orientation. Moreover, in CBTa ceramics with $Cmc2_1$ space group, the polarization can be reorientated along four possible directions: [010], [0$\bar{1}$0], [001], and [00$\bar{1}$]. Assuming that domain switching is fully achieved during the poling process, the polarization of each grain is expected to align along the direction closest to the applied electric field. Consequently, it is reasonable to approximate the piezoelectric response of conventional CBTa ceramics by performing an orientational average over the region nearest to the polarization axis. The detailed methodology is described in our previous work[28]. Among various piezoelectric coefficients, $d_{33}$ is the most critical parameter for evaluating high temperature piezoceramics. For conventional ceramics, the longitudinal piezoelectric coefficient $d_{33,cc}$ can be expressed as:

$$d'_{33} = \cos\theta\sin^2\theta\sin^2\varphi(d_{31}^0 + d_{15}^0) + \cos\theta\sin^2\theta\cos^2\varphi(d_{32}^0 + d_{24}^0) + \cos^3\theta d_{33}^0 \quad (2)$$

View Article Online
DOI: 10.1039/D5MH01252J

$$d_{33,cc} = \frac{\int_0^{\frac{\pi}{2}} \int_0^{\operatorname{arccot}(\cos\varphi)} d_{33}^{'} \sin\theta d\varphi d\theta}{\int_0^{\frac{\pi}{2}} \int_0^{\operatorname{arccot}(\cos\varphi)} \sin\theta d\varphi d\theta} \quad (3)$$

here, $\theta$ and $\varphi$ denote the Euler angles (nutation and precession, respectively) between new and original Cartesian coordinate system. In the following, the case of [100]-textured CBTa ceramics is considered. In the completely textured samples, the out-of-plane piezoelectric coefficient $d'_{33}$ along the [100] direction is expected to be zero, whereas the in-plane $d'_{33}$ should be significantly enhanced. However, since the texturing is achieved via hot forging rather than template grain growth (TGG), the in-plane orientation of the grains remains random, implying that the in-plane [010] and [001] crystallographic directions are still disordered. As a result, the in-plane $d'_{33,\,in}$ can be reduced to a two-dimensional case corresponding to $\varphi = 0$. Accordingly, the $d_{33,tc}$ of the textured ceramics at in-plane can be expressed as:

$$d_{33,in}^{'} = \cos\theta \sin^2\theta (d_{32}^0 + d_{24}^0) + \cos^3\theta d_{33}^0 \quad (4)$$

$$d_{33,tc} = \frac{\int_0^{\frac{\pi}{4}} d_{33,in}^{'} d\theta}{\int_0^{\frac{\pi}{4}} d\theta} \quad (5)$$

Building upon the above discussion, the pure CBTa is selected as a representative example to illustrate the advantages of [100]-textured CBTa ceramics. The piezoelectric tensor and elastic constants of CBTa ceramics are first calculated using density functional perturbation theory (DFPT), with the results summarized in Table 1 and Table 2. Based on these data, the orientational dependence of $d_{33}$ is evaluated using equation (2), as illustrated in Figure 1b. The results reveal a pronounced anisotropy in the $d_{33}$ values of CBTa ceramics, and the $d_{33}$ is plotted as a function of $\theta$ at several $\varphi$ level, which is analogous to the rotated $\theta$ in these planes depicted in Figure 1c. From Figure 1d, the $d_{33}$ values in *bc*-plane ($\varphi = 0$) are significantly higher than those in other planes, indicating the superior piezoelectric performance of [100]-textured CBTa ceramics along the in-plane direction. By applying equations (3) and (5), the longitudinal piezoelectric coefficients of both conventional and [100]-textured CBTa ceramics can be quantitatively determined and are denoted as:

$$d_{33,\,cc} \approx 0.117(d_{31} + d_{15}) + 0.088(d_{32} + d_{24}) + 0.442 d_{33} \quad (6)$$

$$d_{33,\,tc} \approx 0.15(d_{32} + d_{24}) + 0.75 d_{33} \quad (7)$$

As illustrated in Figure 1e, the piezoelectric coefficient of the [100]-textured CBTa

ceramics exhibits a 68% enhancement compared to that of the conventional CBTa ceramics, thereby confirming the effectiveness of the proposed approach. Apparently, the significant improvement of $d_{33}$ in [100]-textured CBTa ceramics can be primarily attributed to the increased contribution from the $d_{24}$ and $d_{33}$ components of corresponding single crystal.

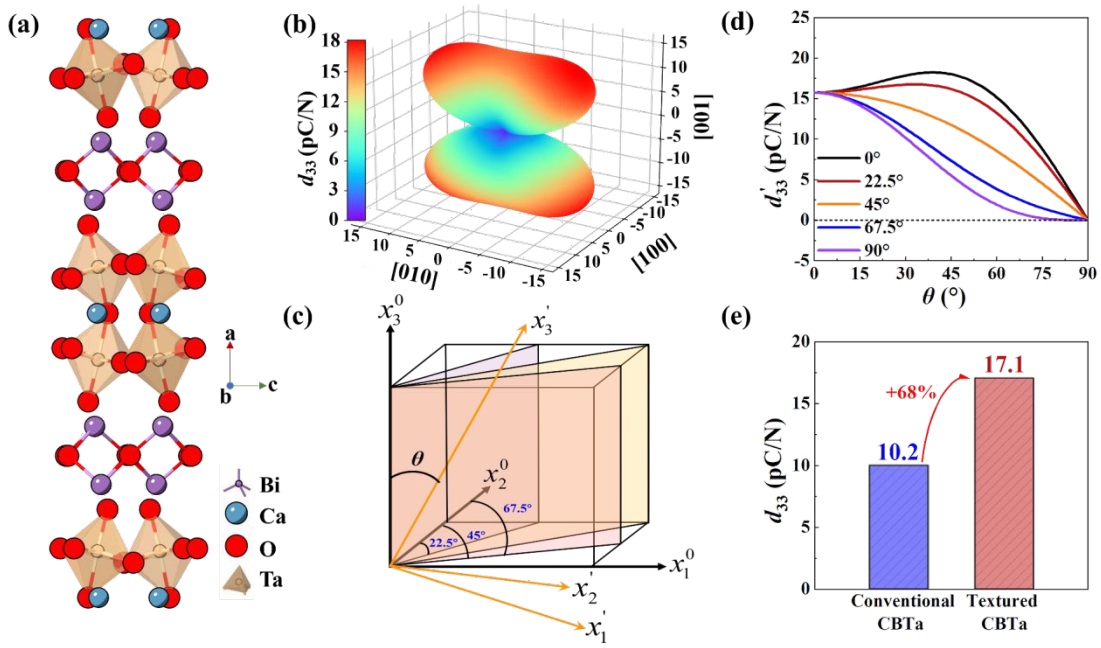


Figure 1 First-principle calculation of the piezoelectricity for CBTa ceramics. (a) Crystal structure of $CaBi_2Ta_2O_9$ ceramics. (b) Orientation dependences of piezoelectric constant $d_{33}$ in $CaBi_2Ta_2O_9$ polycrystal. (c) Schematic showing the orientation varying from [001] to the perpendicular direction via different intermediate planes. (d) Angle (θ)-dependent $d_{33}$ at different $\varphi$ level. (e) Calculated $d_{33}$ values of conventional and [100]-textured $CaBi_2Ta_2O_9$ ceramics.

Table 1 Piezoelectric constants of CBTa, $d$ in unit of pC/N and $e$ in unit of C/m$^2$.

| Materials | $d_{31}$ | $d_{32}$ | $d_{33}$ | $d_{24}$ | $d_{15}$ |
|---|---|---|---|---|---|
| $CaBi_2Ta_2O_9$ | 6.83 | 3.19 | 15.72 | 32.01 | -6.95 |
| Materials | $e_{31}$ | $e_{32}$ | $e_{33}$ | $e_{24}$ | $e_{15}$ |
| $CaBi_2Ta_2O_9$ | 1.47 | 1.81 | 3.27 | 2.79 | -0.37 |

Table 2 Elastic constants of CBTa, $C$ in unit of GPa and $S$ in unit of $10^{-12}$ m$^2$/N.

| Materials | $C_{11}$ | $C_{12}$ | $C_{13}$ | $C_{22}$ | $C_{23}$ | $C_{33}$ | $C_{44}$ | $C_{55}$ | $C_{66}$ |
|---|---|---|---|---|---|---|---|---|---|
| $CaBi_2Ta_2O_9$ | 139.6 | 49.3 | 22.9 | 214.4 | 50.3 | 187.8 | 87.2.4 | 52.5 | 75.4 |
| Materials | $S_{11}$ | $S_{12}$ | $S_{13}$ | $S_{22}$ | $S_{23}$ | $S_{33}$ | $S_{44}$ | $S_{55}$ | $S_{66}$ |
| $CaBi_2Ta_2O_9$ | 7.84 | -1.68 | -0.50 | 5.34 | -1.23 | 5.71 | 11.47 | 19.03 | 13.27 |

Figure. 2a-c show the schematic of testing surface for CNBT-LC(CS), CNBT-LC(//) and CNBT-LC(⊥) ceramics during XRD characterization, respectively, and the

XRD patterns of all ceramics are represented in Figure 2d. All diffraction peaks are indexed to the phase structure of pure $CaBi_2Ta_2O_9$ ($Cmc2_1$), and no second phase is detected. This confirms that $(Li_{0.5}Ce_{0.5})^{2+}$ and $(Na_{0.5}Bi_{0.5})^{2+}$ dopant ions incorporate into the CBTa lattice, forming a stable solid solution. The dominant diffraction peak at (511) aligns with the characteristic ($\underline{2m+1}11$) peak of BLSFs[29]. Importantly, hot-forged CNBT-LC ceramics exhibit anisotropic diffraction behavior: (00*l*), (*h*00) and (0*k*0) diffraction peaks show pronounced orientation dependence (see Figure 2d). For CNBT-LC(⊥), the intensity of (002)/(020) peaks are significantly higher than that of CNBT-LC(//), as shown in Figure 2e. Whereas CNBT-LC(//) ceramics display enhanced (600), (800), and ($\underline{10}00$) peaks. This indicates that preferential grain orientation: (l00)-textured growth in CNBT-LC(//) and (00*l*)/(0*k*0)-random orientation in CNBT-LC(⊥). Bismuth-layered-structured ferroelectric ceramics with $Cmc2_1$ space group exhibit a significantly higher grain growth rate along the *b* and *c*-axis of the unit cell than along the *a*-axis. Consequently, their grains display a distinct anisotropic morphology: the length/width is much larger than the thickness, resulting in a large flake-like shape. In the unit cell coordinate system, the area of the *bc*-plane is far larger than that of the *ab* or *ac* planes. In pre-sintered CNBT-LC ceramic pillars, grains are randomly distributed with no preferred orientation. However, during hot forging, as the pre-sintered ceramic softens at high temperature, the *bc*-plane—compared with the *ab*/*ac* planes—rotates more readily to a state perpendicular to the external stress during plastic compressive deformation, thus forming a textured structure.

It is worth mentioning that hot-forging temperature influences grain orientation. As depicted in Figure 2f-g, $I_{(800)}/I_{(511)}$ and $I_{(\underline{10}00)}/I_{(511)}$ ratios for CNBT-LC(1200//) are higher than those of CNBT-LC(1180//), indicating stronger [100] texture in samples hot-forged at 1200 °C compared to 1180 °C. The degree of grain orientation in textured ceramics is quantified by the Lotgering factor (*f*) as follows[30]:

$$f = \frac{P - P_0}{1 - P_0}, \tag{8}$$

$$P = \frac{\sum I(00l)}{\sum I(hkl)}, \tag{9}$$

$$P_0 = \frac{\sum I_0(00l)}{\sum I_0(hkl)}, \tag{10}$$

where $I_0$ and $I$ denote the XRD intensities of non-oriented CNBT-LC(1150CS) and

textured CNBT-LC(//) ceramics, respectively. $P_0$ and $P$ represent the normalized XRD intensities of ($h$00) crystal planes for the non-oriented and textured samples, respectively. The calculated $f$ values of CNBT-LC(1180//) and CNBT-LC(1200//) ceramics are 0.338 and 0.404, respectively. Compared with RTGG and TGG techniques, the textured ceramics prepared by hot forging exhibit a relatively lower degree of orientation. However, we propose that the degree of texture can be further enhanced by regulating hot forging pressure, temperature, and duration, with the underlying mechanism as follows: First, driven by the applied pressure, the *bc* crystal planes of grains within pre-sintered ceramic pillars tend to rotate and rearrange along a direction perpendicular to the pressure. Increasing the hot forging pressure can induce greater compressive deformation in pre-sintered ceramic pillars, thereby enhancing the extent of grain rotation and rearrangement. Second, higher hot forging temperatures can enhance the plasticity of pre-sintered ceramic pillars, reducing the resistance to grain rotation and rearrangement and thus facilitating an improvement in the degree of orientation. Furthermore, rearranged grains can act as templates to induce oriented growth in non-rearranged grains (whose *bc* crystal planes are not perpendicular to the direction of the applied pressure). Prolonging the hot forging duration and appropriately increasing the hot forging temperature can facilitate the full progression of this oriented growth process, thereby further enhancing the degree of texture.

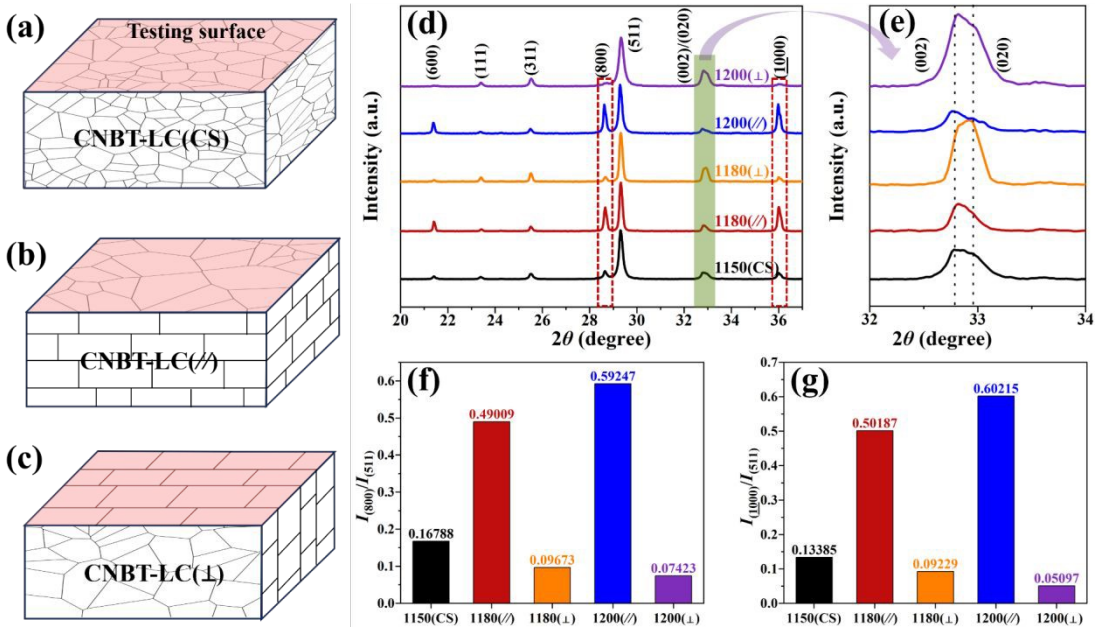


Figure 2 The crystal of CNBT-LC ceramics. (a-c) The testing surfaces of CNBT-LC(CS), CNBT-LC(//) and CNBT-LC(⊥) ceramics during XRD characterization, respectively. (d) XRD patterns of CNBT-LC(1150CS), CNBT-LC(1180//), CNBT-LC(1180⊥), CNBT-LC(1200//) and CNBT-

View Article Online
DOI: 10.1039/D5MH01252J

LC(1200⊥) ceramics. (e) (002) and (020) peaks of all the samples. (g-f) The ratios of $I_{(800)}/I_{(115)}$ and $I_{(\underline{1}000)}/I_{(511)}$.

Scanning electron microscopy (SEM) images from Figure 3a-e reveal the microstructure of CNBT-LC ceramics. Based on the grain growth feature of BLSFs compounds, it can be inferred that the quasi-equiaxed platelet-like morphologies (dominated in Figure 3a-c observed in CNBT-LC(1180//) and CNBT-LC(1200//) ceramics correspond to the *bc* crystal plane (perpendicular to the a axis), whereas the narrow elongated morphologies (dominated in Figure 3b-d) shown in CNBT-LC(1180⊥) and CNBT-LC(1200⊥) ceramics correspond to the *ac* or *bc* crystal plane(perpendicular to the *b* or *a* axis) [31]. For CNBT-LC(1150CS) ceramics in Figure 3e, it features equiaxial plate-like planes and narrow elongated planes. It should be noted that intergranular pores are observed in all samples, but less in the hot forged samples. The densities of all samples were measured by Archimedes' law, as shown in Figure 3f. Compared with conventionally sintered ceramics, hot-forged sintered ceramics exhibited higher density, and it increased with increasing hot-forging temperature. Furtherly, electron backscatter diffraction (EBSD) was conducted to characterize the crystallographic texture of the CNBT-LC(1200//) and CNBT-LC(1200⊥) samples in detail, as shown in Figure 3g-i. Figure 3g-h show the natural grain morphology of sample CNBT-LC(1200//) and CNBT-LC(1200⊥), which resemble those in Figure 3c-d. According to the EBSD patterns and inverse pole in Figure 3i-j, it can be seen that (*h*00) orientation is dominant in CNBT-LC1200(//), while (010) and (001) orientations dominate in CNBT-LC1200(⊥), which is consistent with the XRD analysis.

View Article Online
DOI: 10.1039/D5MH01252J



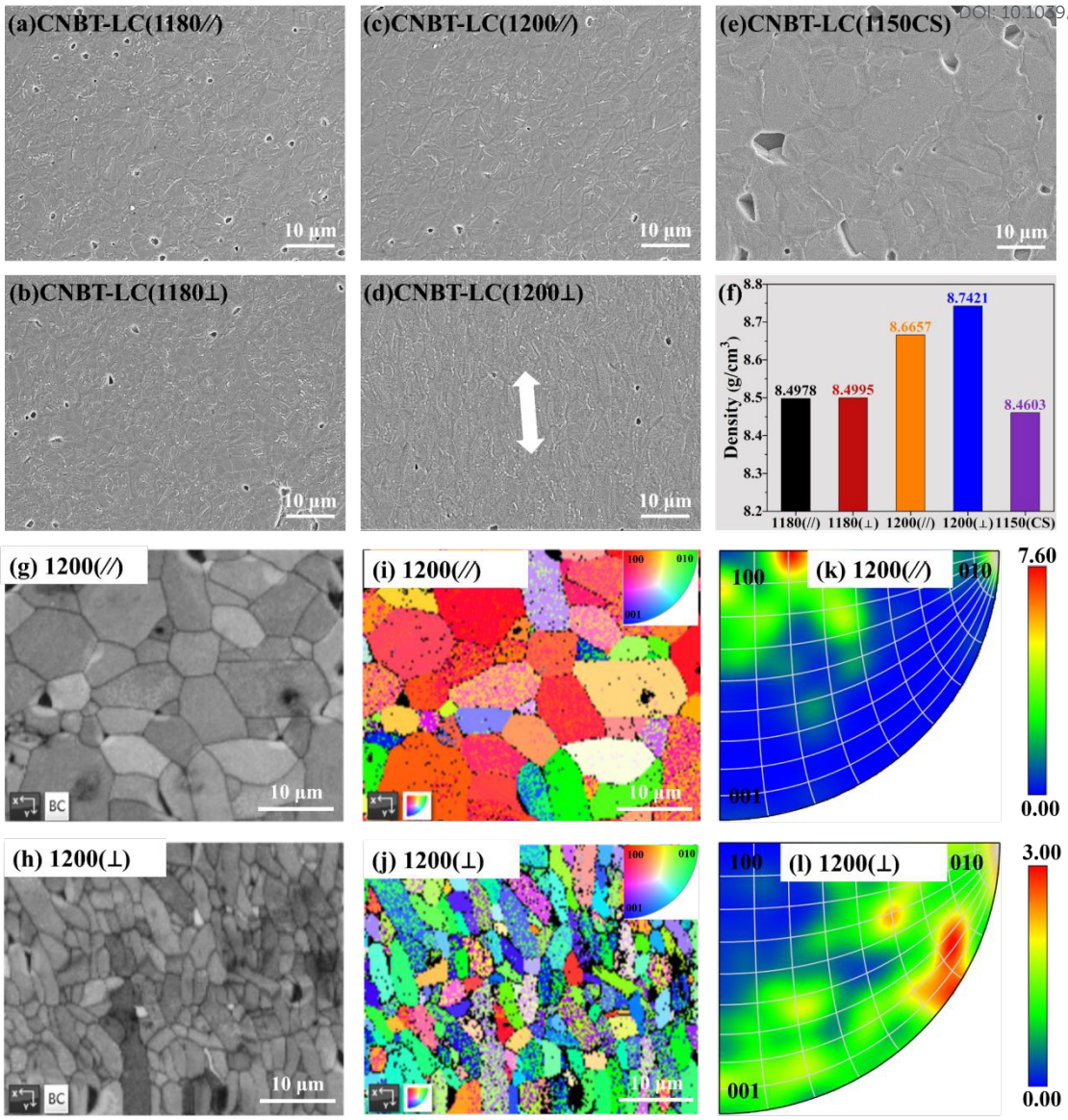


Figure 3 Grain orientation of CNBT-LC ceramics. (a-e) SEM images of the polished thermally etched surfaces for CNBT-LC(1180//), CNBT-LC(1180⊥), CNBT-LC(1200//) and CNBT-LC(1200⊥) ceramics; (f) the densities of all CNBT-LC ceramics. (g-h) The grain morphology of CNBT-LC(1200//) and CNBT-LC(1200⊥) ceramics. (i-j) Phase orientation mappings of CNBT-LC(1200//) and CNBT-LC(1200⊥) ceramics. (k-l) Inverse pole Figures CNBT-LC(1200//) and CNBT-LC(1200⊥) ceramics.

To distinguish the contributions of grains and grain boundaries to conductive behavior, the complex impedance spectra of all samples were measured, as shown in Figure 4a-c. The exclusive presence of single Cole-Cole semicircles in the complex impedance spectra of all samples confirms that contributions from grain interiors dominate the governing of electrical behavior. The progressive reduction in semicircular radii observed with increasing temperature from 500 °C to 750 °C directly correlates with decreased resistance, reflecting enhanced ionic conduction at elevated

temperatures. Notably, the radii of Cole-Cole semicircles for CNBT-LC(1200//) are significantly larger than those of CNBT-LC(1200⊥) at the same temperature, indicating higher resistance in CNBT-LC(1200//). This may be attributed to the reduction in grain boundary conductivity caused by the preferential grain orientation. Additionally, the complex electric modulus ($M^*$) was employed to understand the conduction relaxation process[32] :

$$M^* = \frac{1}{\varepsilon^*} = \mathrm{j}\omega\varepsilon_0 Z^* = M' + M'' \tag{11}$$

The frequency dependence of the normalized imaginary part of electric modulus ($M''/M''_{\max}$) for CNBT-LC(1150CS), CNBT-LC(1200//) and CNBT-LC(1200⊥) samples are shown in Figure 4d-f, respectively. A single peak is observed at different temperatures for CNBT-LC(1150CS), CNBT-LC(1200//) and CNBT-LC(1200⊥) ceramics, corresponding to the grain interior, with the regions on either side of the peak representing two distinct relaxation processes. Below the $M''$ peak, charge carriers exhibit long-range mobility, whereas above the $M''$ peak, their movement is confined to shorter distances. However, the $M''$ peaks of CNBT-LC1200(⊥) gradually broaden in the high temperature regions and tend to form multiple relaxation peaks, which may be caused by the grain boundary effect mentioned above. As the temperature increases, the $M''$ peak gradually shifts to higher frequencies, demonstrating that the non-Debye relaxation processes in CNLCBT ceramics are temperature-dependent. To further investigate the relaxation process, the activation energy($E_{\mathrm{relax}}$) of CNLCBT ceramics can be determined using the following equation:[33]

$$f_p = f_0 \exp(-\frac{E_{relax}}{k_B T}) \tag{12}$$

Where $f_{\mathrm{p}}$ represents the frequency according to the peak of $M''_{max}$, $k_{\mathrm{B}}$ is the Boltzmann constant, $f_0$ is the attempted jump frequency and $T$ is temperature (K). The linear fitting processes of CNBT-LC1150(CS), CNBT-LC1200(//) and CNBT-LC1200(⊥) ceramics are shown in the Figure 4g-i. As displayed, the $E_{\mathrm{relax}}$ values for CNLCBT ceramics range from 1.74 eV to 1.79 eV. This behavior is primarily attributed to conduction via localized defect states especially oxygen vacancy migration instead

of intrinsic band-to-band transitions, which require energies on the order of the band gap (3.0 eV–3.4 eV). After hot forging, the increase in $E_{relax}$ to 1.79 eV is likely due to process-induced densification, grain orientation and defect passivation. These modifications reduce both the concentration and mobility of oxygen vacancies, thereby elevating the energy barrier for charge carrier migration and shifting the conduction mechanism toward a more ordered state. It is reported that oxygen vacancy defects tailoring is an effective strategy to boost massive ferroelectric domains and enhance electrical properties of BLSFs[34-40].

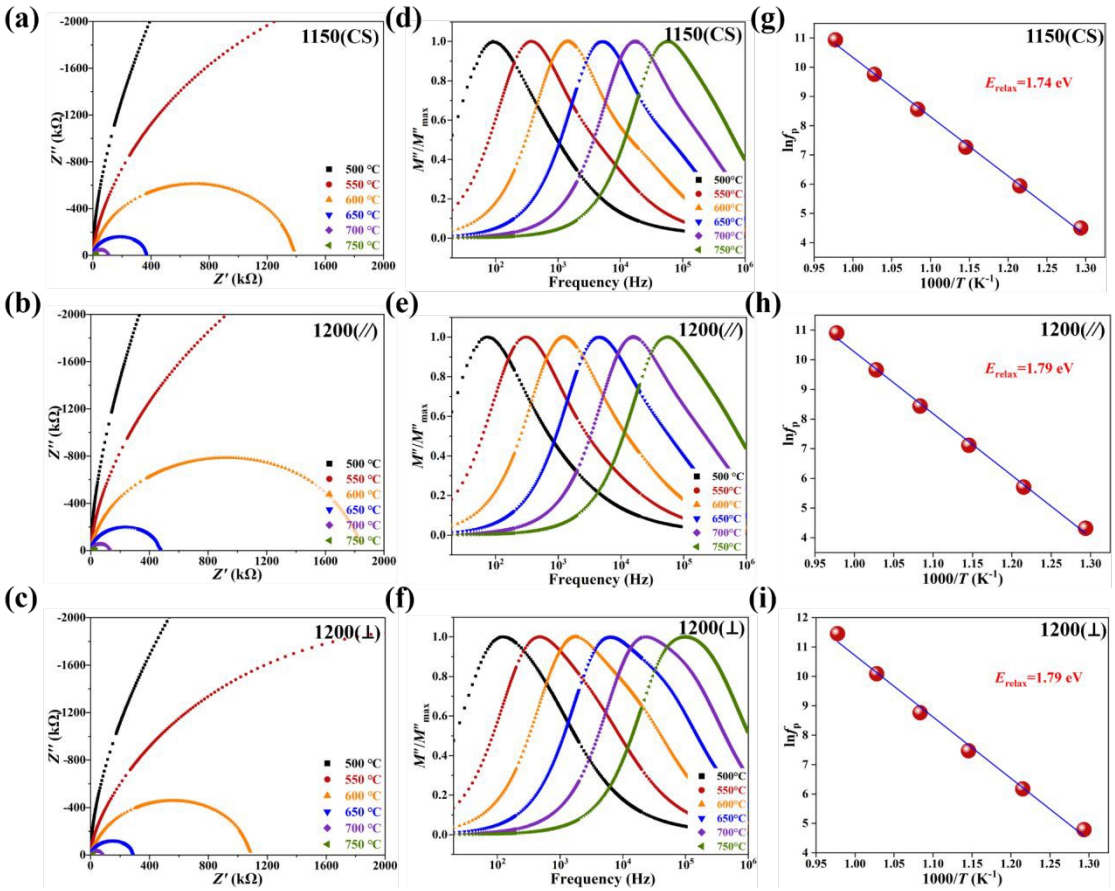


Figure 4 Impedance characteristics of CNBT-LC ceramics. (a-c) Impedance plots of the CNBT-LC(1150CS), CNBT-LC(1200//) and CNBT-LC(1200⊥) ceramics. (d-f) Normalized imaginary part of the electric modulus ($M''/M''_{max}$) as a function of frequency for the CNBT-LC(1150CS), CNBT-LC(1200//) and CNBT-LC(1200⊥) ceramics with different temperatures from 500 °C to 750 °C. (g-i) Activation energy of the relaxation process ($E_{relax}$) of the CNBT-LC(1150CS), CNBT-LC(1200//) and CNBT-LC(1200⊥) ceramics.

As is well known, the piezoelectric response of ferroelectrics originates from intrinsic (lattice structure) and extrinsic (domain structure) contributions. Herein, the domain morphologies of CNBT-LC(1150CS), CNBT-LC(1200//) and CNBT-

LC(1200⊥) were investigated using the vertical piezoresponse force microscopy (VPFM), as displayed in Figure 5a-c. In the tested samples, isolated strip domains were observed. When compared to CNBT-LC(1150CS), CNBT-LC(1200//) and CNBT-LC1200(⊥) exhibit more regular domain morphologies, with the long edges of their domains nearly parallel to each other. CNBT-LC1200(//) displays the largest domain width, while CNBT-LC1200(⊥) exhibits the smallest value. Furthermore, within the same dimensional region, CNBT-LC(1200⊥) exhibits a higher domain density, whereas CNBT-LC1200(//) shows the lowest value of this parameter. In ferroelectric ceramics, the motion of domain walls significantly influences the electrical properties of materials. Generally, a reduction in domain size leads to an increase in total domain wall energy, thereby enhancing the mobility of domain walls and promoting the improvement of piezoelectric performance[41]. In addition, ferroelectric properties can also reflect the piezoelectric activity of ferroelectrics to a large extent. Figure 5d illustrates the variation of spontaneous polarization intensity with electric field (*P*-*E*) for all samples. The remanent spontaneous polarization $P_r$ of CNBT-LC(⊥), featuring *b*/*c*-axis-oriented grains, is significantly higher than that of other samples, while CNBT-LC(//) with *a*-axis-oriented grains shows the lowest $P_r$. Owing to the fact that high temperature hot-forging facilitates oriented grain growth, CNBT-LC1200(⊥) displays the maximum $P_r$ of approximately 16.37 μC/cm². This value represents a 458.7% increase compared to CNBT-LC(1150CS) with unoriented grains ($P_r$~2.93 μC/cm²).

Notably, all *P*-*E* curves exhibit asymmetric shapes. The asymmetric hysteresis loops may arise from the directional polarization of defect dipoles. According to Teranishi et al., the defect dipoles consist of oxygen vacancies ($V_O^{\cdot\cdot}$) and negatively charged defects (e.g., cation vacancies $V_{Bi}'''$ and $V'_{\mathrm{Na}}$). The specific formation equations are provided as follows:

$$Bi_2O_3 \rightarrow 2Bi(g)\uparrow + \frac{3}{2}O_2(g)\uparrow + 2V_{Bi}''' + 3V_O^{\cdot\cdot} \quad (13)$$

$$Na_2O \rightarrow 2Na(g)\uparrow + \frac{1}{2}O_2(g)\uparrow + 2V_{Na}' + V_O^{\cdot\cdot} \quad (14)$$

Generally, the internal bias field ($E_{ibf}$) arises from the reorientation of defect-dipoles under an external electric field. When the ceramics are poled, the spontaneous polarization ($P_s$) switches to the poling direction, and defect dipoles ($P_d$) form with the orientations aligned along $P_s$. Consequently, the $E_{ibf}$—parallel to the poling direction—is induced by the $P_d$ in piezoelectric ceramics. When the applied electric field opposes $E_{ibf}$, it must overcome the combined effect of coercive field ($E_c$) and ($E_{ibf}$) to enable

domain switching, i.e., $E_c^+ > E_c^-$. In this work, the weak asymmetry of the *P*-*E* loop is primarily attributed to the $E_{ibf}$, generated by reorientated defect dipoles $(V_{Bi}''' - V_O^{\cdot\cdot})'$ and $(V_{Na}' - V_O^{\cdot\cdot})^{\cdot}$. Owing to the unique compositional configuration of bismuth layered structure ferroelectrics (BLSFs), Bi vacancies $V_{Bi}'''$ and oxygen vacancies $V_O^{\cdot\cdot}$ are unavoidable, and similar phenomena were observed in CBN, CBTa, CBT and BIT based ceramics.[23, 25, 42-44]

Figure 5e depicts the polarization current as a function of electric field for all samples. CNBT-LC(1200⊥) displays the highest polarization switching current (0.281 mA), attributed to the largest population of fully switchable spontaneous polarizations, whereas CNBT-LC(1800//) exhibits the lowest value (0.01 mA), owing to the minimal number of such switchable dipoles. In summary, due to the optimization of the domain configuration and enhanced remanent polarization, the piezoelectric properties of textured CNBT-LC(⊥) ceramics are expected to be improved.

Figure 5f shows the depoling temperature dependence of the piezoelectric coefficient $d_{33}$ of CNBT-LC ceramics from room temperature to 950 °C. For CNBT-LC(1150CS), the $d_{33}$ value at room temperature is approximately 12.7 pC/N, close to the value (13.5 pC/N) previously reported by us[45]. For CBTa ceramics with the $Cmc2_1$ space group, their spontaneous polarization is along the *b*-axis or *c*-axis of the unit cell, whereas the *a*-axis is a non-polar axis, which endows them with anisotropic properties. Along the direction of the poling electric field, the grains in the CNBT-LC (⊥) sample exhibit preferred orientation characteristics along the *b*-axis or *c*-axis, whereas the CNBT-LC (//) sample exhibits preferred orientation characteristics along the *a*-axis, as shown in Figure 5g. Thus, compared with the CNBT-LC (//) sample, there are more spontaneous polarizations in the CNBT-LC (⊥) sample that can be reversed with the poling electric field, thereby exhibiting more excellent piezoelectric properties. Consequently, CNBT-LC(⊥) demonstrates the highest piezoelectric performance, with a $d_{33}$ value exceeding 18 pC/N, while CNBT-LC(//) shows the weakest piezoelectric properties ($d_{33}$ < 10 pC/N). A proper increase in hot forging temperature can render the pre-sintered ceramic pillars “softer” in texture, thereby reducing the resistance to rearrangement and orientation of crystal grains during their plastic deformation. Ultimately, this enhances the degree of orientation, further improving the piezoelectric properties of the material. Specifically, $d_{33}$ of CNBT-LC(1200⊥) ceramics reaches up to 21.8 pC/N，which is a 71% improvement over CNBT-LC(1150CS) ceramics. To the best of our knowledge, this represents the highest $d_{33}$ value currently reported for CBTa

based high-temperature piezoelectric ceramics. Unfortunately, due to the equipment's maximum heating temperature being limited to 1200 °C, experimental work under higher hot forging temperature conditions cannot be conducted. Furthermore， the $d_{33}$ values of all samples exhibit a slight decrease with increasing temperature. Notably, the $d_{33}$ values remain relatively stable until the depoling temperature exceeds 600 °C. Above this threshold, $d_{33}$ undergoes a sharp decline and diminishes to zero when the temperature reaches 920 °C. It should be noted that even at a depoling temperature $T_d$ of 900 °C, the piezoelectric constant $d_{33}$ of CNBT-LC(1200⊥), CNBT-LC(1180⊥) and CNBT-LC(1150CS) retains at least 90% of their initial values. Particularly, for CNBT-LC1180(⊥), CNBT-LC1200(⊥), the reductions in $d_{33}$ values are only 7% and 5%, respectively. It indicates that hot-forged CNBT-LC ceramics exhibit excellent resistance to thermal depolarization.

High-temperature resistivity is a critical metric for evaluating the thermal stability of piezoelectric material in extreme heat environments. Figure 5h shows the *dc* resistivity ($\rho$) of CNBT-LC ceramics as a function of temperature. Compared with the hot-forged samples, the dc resistivity of CNBT-LC(1150CS) is significantly lower. When the temperature reaches 600 °C, its *dc* resistivity is approximately $1.92\times10^6$ Ω·cm, while that of the hot-forged sample exceeds $1\times10^7$ Ω·cm. The possible reasons are as follows: (1) The hot-forged samples possess a higher density, as shown in Figure 1f; (2) the hot-forged samples exhibit finer grain size and a larger proportion of grain boundaries, which hinder the migration of charge carriers. It is worth mentioning that the $d_{33}$ values of CNBT-LC(⊥) ceramics in this work are superior compared with other reported CBTa, $CaBi_2Nb_2O_9$ (CBN) and $Bi_3TiNbO_9$ (BTN) based ceramics with high $T_C$ (>900 °C, together with the ultra-high DC resistivity at 600 °C, as shown in Figure 5i [19, 23, 25, 26, 46-54]. Figure 5j shows the temperature dependence of relative dielectric constants ($\varepsilon_r$) of the conventional sintered and hot forged samples, which were measured at 1 MHz. Within the tested temperature range, all samples exhibit a dielectric anomaly peak around 922 °C, which corresponds to the ferroelectric-paraelectric phase transition[45]. Since CNBT-LC (⊥) is oriented along the *bc*-plane (with spontaneous polarization $P_s$ parallel to the *b/c* axes) and CNBT-LC (//) is oriented along the *ab*- or *ac*-plane, the former thus has a higher domain density than the latter and consequently a larger polarizability, and thereby exhibits a higher relative permittivity. Thus, such anisotropy in relative permittivity stems primarily from the texturing of the microstructure. It is also reasonable that the relative dielectric constant of CNBT-

LC(1150CS) is greater than that of CNBT-LC(//) but smaller than that of CNBT-LC(⊥).

In summary, the anisotropic characteristics exhibited in the properties of CNBT-LC (//) and CNBT-LC (⊥) confirm that hot forging enables the texturing of the microstructure of CBTa-based high-temperature piezoelectric ceramics, with their comprehensive performance being superior to that of traditionally sintered ceramics. The hot forging method is an effective strategy to enhance the performance of piezoelectric ceramics, and it is particularly more effective for materials with strong anisotropy in grain morphology.

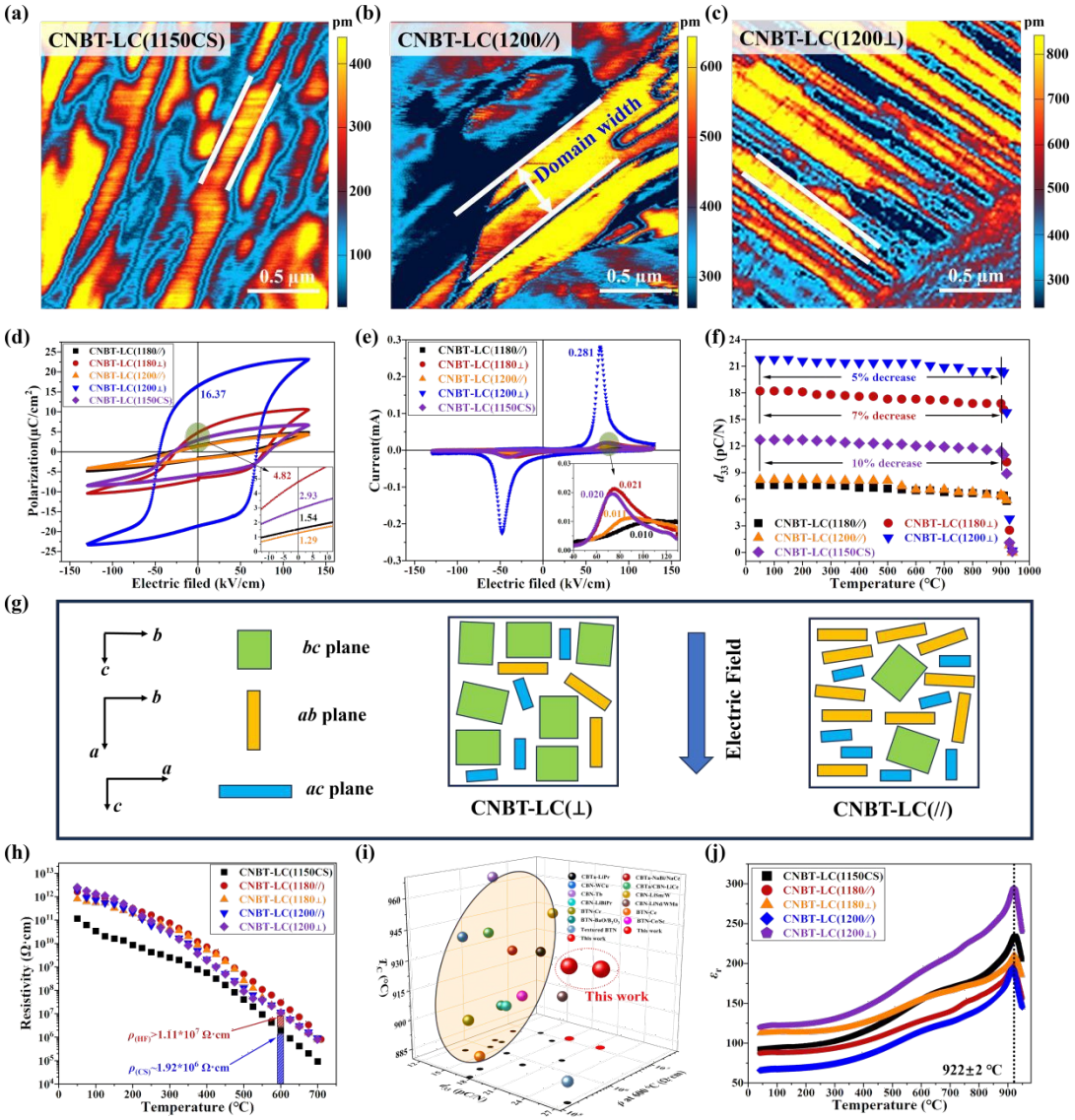


Figure 5 Domain structure and electrical performances of CNBT-LC ceramics. (a-c) Vertical PFM amplitude images of CNBT-LC1150(CS), CNBT-LC1200(//) and CNBT-LC1200(⊥) ceramics, respectively. (d-e) *P-E* and *I-E* hysteresis loops measured at 180 °C and 1 Hz. (f) Thermal depolarization of $d_{33}$ values for CNBT-LC ceramics. (g) Schematic diagram of the relationship between the poling electric field and the preferred orientation of grains in CNBT-LC(⊥) and CNBT-LC(//) ceramics. (h)Temperature dependence of DC resistivity ($\rho$) of CNBT-LC ceramics. (i) A

comprehensive comparison of $d_{33}$ values, $T_C$ and $\rho$ at 600 °C for CBTa, CBN and BTN based ceramics. (j) temperature dependence of relative permittivity($\varepsilon_r$) for all ceramics.

## 3. Conclusion

Textured CBTa based ceramics with one single phase are prepared by hot forging method. XRD and EBSD analyses show that hot-forged CNBT-LC ceramics perform the typical characteristics of textured ceramics. And the Lotgering factor increases from 33% to 40% with forging temperature increase from 1180 °C to 1200 °C. Hot forging induces high densities and limits oxygen vacancy migration, leading to an increase in activation energy from 1.74 eV to 1.79 eV. The $d_{33}$ values of CNBT-LC1180(⊥) (18.2 pC/N) ceramics are improved by 43% compared to CNBT-LC1150 (CS) (12.7 pC/N) ceramics, while CNBT-LC1200(⊥) (21.8 pC/N) ceramics are increased by 72%. Notably, CNBT-LC1200(⊥) ceramics exhibit excellent thermal stability ($d_{33}$ values decreases only 5% of its initial value after annealing at 900 °C, ultrahigh $T_C$ (922 °C) and outstanding DC resistivity ($\rho$~$1.11\times10^7$ Ω·cm at 600 °C, demonstrating the potential competitiveness in the field of high temperature piezoelectric sensors. The hysteresis loops of hot-forged CNLCBT ceramics with texture show that the $P_r$ and $I_{max}$ values exhibit the same anisotropy as the piezoelectric properties, i.e., the CNBT-LC(⊥) ceramics show higher $d_{33}$, $P_r$ and $I_{max}$ values compared with CNBT-LC(//) ceramics, which are due to the grain orientation-induced alignment of the $P_s$ with lower domain switching energies. Finally, it is verified by VPFM that the reduction of domain size and the regular arrangement of the domains are important reasons for the enhanced piezoelectric and ferroelectric performances of CNBT-LC1200(⊥) ceramics. This study establishes a viable pathway for optimizing electrical performance through crystallographic texturing and demonstrates that the developed hot forging methodology serves as a robust processing route for the fabrication of textured BLSFs. The observed enhancement mechanism suggests that targeted refinement of thermomechanical parameters, particularly strain rate and temperature gradients, could enable precise control of domain alignment kinetics, potentially yielding BLSFs with superior crystallographic orientation and enhanced electromechanical response.

## 4. Experimental Section

$Ca_{0.5}(NaB(i)_{0.23}(LiC(e)_{0.02}Bi_2Ta_2O_9$ (CNBT-L(C) ceramics are first synthesized by solid-phase method. The raw materials and the preparation process can be found in our previous work[45]. The conventional sintered (at 1150 °C for 4 h) ceramics with random orientation can be denoted as CNBT-LC (1150CS). Regarding the hot-forging process,

the conventionally sintered bodies are placed into the $Al_2O_3$ mould with carbon paper and sintered in the HF furnace at 1180 °C and 1200 °C for 4 h, with a pressure of 15 MPa applied for 1 h, respectively. The hot-forging processes are shown in Figure 6a. Subsequently, the hot-forged ceramics are calcined at 1000 °C for 2 h to remove the infiltrated carbon. Finally, the samples are cut parallel and perpendicular to the pressure direction, respectively. Based on the relationship between the test direction and pressure direction of the samples, the samples are abbreviated as CNBT-LC (//) and CNBT-LC (⊥), as shown in Figure 6b.

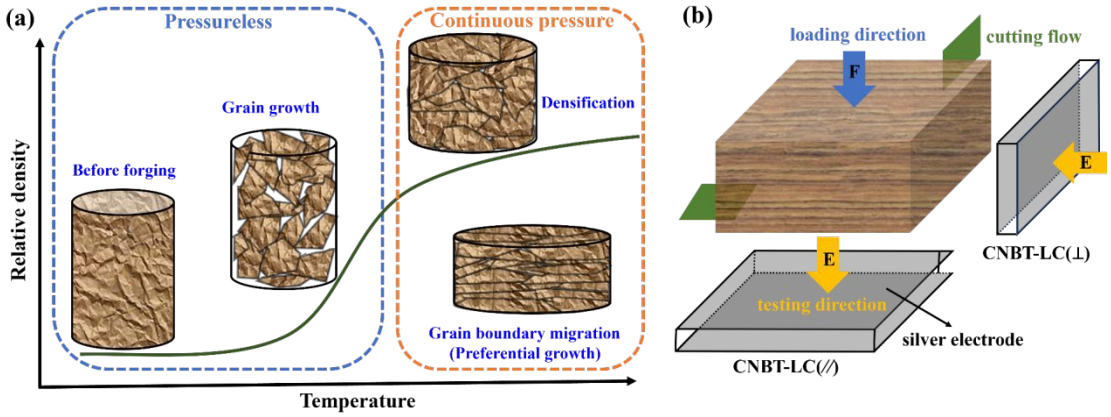


Figure 6 Hot forging process of CNBT-LC ceramics. (a) Preferential grain growth in Hot forging process. (b) Cutting schematic and sample definition of hot forged CNBT-LC ceramics

The phase structure of the sample is measured in the $2\theta$ range from 20° to 60° by an X-ray diffractometer (XRD, Holland EMPYREAN) using CuKα radiation. The microstructure of ceramics can be observed by a scanning electron microscope (SEM). All ceramics, including CNBT-LC(1150CS), CNBT-LC(1180//), CNBT-LC(1180⊥), CNBT-LC(1200//) and CNBT-LC(1200(⊥) ceramics, are coated with silver (A(g) and polarized in silicone oil at 220 °C under an electric field of 12 kV/mm for about 20 min. The $d_{33}$ values of the polarized ceramics are measured using a quasi-static $d_{33}$ tester (ZJ 3A, Institute of Acoustics). The *P-E* and *I-E* curves of the ceramics are measured by a ferroelectric analyzer (Radiant Precision Premier II, Radiant Technologies). The direct current (*dc)* resistivity is measured by a high-resistance meter at 10 V with a temperature range of 200 °C~700 °C and a temperature interval of 25 °C. The impedance data are measured using LCR tester. The temperature dependence of dielectric constant ($\varepsilon_r$) and dielectric loss (tan$\delta$) of the samples is measured by LCR instrument. The polarized samples are annealed at different temperatures, ranging from room temperature (RT) to 950 °C, for 2 h, and the corresponding piezoelectric constants are measured at RT. The domain structure of CNBT-LC ceramics is characterized by

View Article Online
DOI: 10.1039/D5MH01252J

PFM with commercial microscopy (MFP-3D, Asylum Research).

The first principle calculations are performed using the Vienna Ab-initio Simulation Package (VASP) based on density functional theory (DFT)[55]. The exchange-correlation functional is treated within the generalized gradient approximation (GGA) using a revised Perdew-Burke-Ernzerhof functional for solid (PBEsol)[56]. The projector augmented-wave (PAW) potential is employed to describe the electron-ion interaction[57], and the Ca $3s^2 3p^6 4s^2$, Bi $5d^{10} 6s^2 6p^3$, Ta $5p^6 6s^2 5d^3$, and O $2s^2 2p^4$ states are treated as valence electrons in the calculations. The wave function is expanded in plane waves, truncated at a cut-off energy of 520 eV. Geometry optimizations are considered converged when the residual force of each atom was less than 0.002 eV/Å. Brillouin zone sampling is performed using a Γ-centered *k*-point mesh with a grid spacing of $0.04 \times 2\pi$ Å$^{-1}$ for Brillouin zone sampling were chosen. Elastic and piezoelectric constants are as the second derivatives of total internal energy are extracted by density functional perturbation theory (DFPT) combined with finite differences method[58].

**Author contributions**

Wei Shi conceived and designed experiments and wrote manuscripts. Mingyue Mo carried out PFM characterization. Qi Hu conducted the XRD measurements. Zhi Tan contributed to the theoretical calculation section. Shangyi Guan and Liang Xu analyzed the data. Jie Xing supervised the project. Wei Shi and Qiang Chen led the manuscript preparation with contributions from all authors.

**Conflict of Interest**

The authors declare no conflict of interest.

**Data Availability Statement**

The data that support the findings of this study are available from the corresponding author upon reasonable request.

**Acknowledgment**

This work was supported by National Natural Science Foundation of China (No. 51932010), Applied Basic Research of Sichuan Province (No.2020YJ0317) and the Fundamental Research Funds for Central Universities. The authors also thank Xiaoshan Zhang for his help with SEM images from the lab of center of the college of materials science and engineering in Sichuan University.

View Article Online
DOI: 10.1039/D5MH01252J

View Article Online
DOI: 10.1039/D5MH01252J





**Reference**


1. C. Qiu, B. Wang, N. Zhang, S. Zhang, J. Liu, D. Walker, Y. Wang, H. Tian, T. R. Shrout, Z. Xu, L. Q. Chen and F. Li, *Nature*, 2020, **577**, 350-354.
2. X. Li, L. Zhu, P. Huang, Z. Chen, W. Bai, L. Li, F. Wen, P. Zheng, W. Wu, L. Zheng and Y. Zhang, *J. Appl. Phys.*, 2020, **127,** 044102.
3. Y. Hioki, M. Costantini, J. Griffin, K. C. Harper, M. P. Merini, B. Nissl, Y. Kawamata and P. S. Baran, *Science*, 2023, **380**, 81-87.
4. L. Xu, J. Lin, Y. Yang, Z. Zhao, X. Shi, G. Ge, J. Qian, C. Shi, G. Li, S. Wang, Y. Zhang, P. Li, B. Shen, Z. Fu, H. Wu, H. Huang, F. Li, X. Ding, J. Sun and J. Zhai, *Nat. Commun.*, 2024, **15**, 9018.
5. H. C. Thong, Z. Li, J. T. Lu, C. B. Li, Y. X. Liu, Q. Sun, Z. Fu, Y. Wei and K. Wang, *Adv. Sci. (Weinh)*, 2022, **9**, 2200998.
6. B. Wu, L. Zhao, J. Feng, Y. Zhang, X. Song, J. Ma, H. Tao, Z. Xu, Y. X. Liu, S. Wang, J. Lu, F. Zhu, B. Han and K. Wang, *Nat. Commun.*, 2024, **15**, 2408.
7. M. Sun, P. Li, J. Du, W. Han, J. Hao, K. Zhao, H. Zeng and W. Li, *J. Materiomics*, 2022, **8**, 288-294.
8. Q. Guo, X. Meng, F. Li, F. Xia, P. Wang, X. Gao, J. Wu, H. Sun, H. Hao, H. Liu and S. Zhang, *Acta Mater.*, 2021, **211**, 116871.
9. C. Pan, G. Zhao, S. Li, X. Wang, J. Wang, M. Tao, X. Zhang, C. Yang, J. Xu, W. Yin, L. Yin, W. Song, P. Tong, X. Zhu, J. Yang and Y. Sun, *J. Mater. Chem. C*, 2022, **10**, 15851-15860.
10. Y. Cheng, S. Guan, Q. Wang, X. Wu, J. Xing, L. Jiang, Z. Tan and J. Zhu, *J. Eur. Ceram. Soc.*, 2024, **44**, 6978-6986.
11. H. Li, N. Chen, J. Xing, H. Chen, Z. Tan, M. Mo, Q. Chen, J. Zhu, F. Li, Z. Liu, W. Ouyang and H. Zhu, *J. Mater. Chem. C*, 2024, **12**, 1809-1819.
12. D. Zhang, D. Sando, P. Sharma, X. Cheng, F. Ji, V. Govinden, M. Weyland, V. Nagarajan and J. Seidel, *Nat. Commun.*, 2020, **11**, 349.
13. J. Yin, C. Zhao, Y. Zhang and J. Wu, *Acta Mater.*, 2018, **147**, 70-77.
14. Q. Guo, F. Li, F. Xia, X. Gao, P. Wang, H. Hao, H. Sun, H. Liu and S. Zhang, *ACS Appl. Mater. Interfaces*, 2019, **11**, 43359-43367.
15. H. Chen, Y. Xie, J. Xi, W. Zhuang, W. Wang, J. Xing, H. Liu and J. Zhu, *J. Mater.Chem. A*, 2023, **11**, 25945-25954.
16. X. Xie, Z. Zhou, R. Liang and X. Dong, *Adv. Elec. Mater.* , 2022, **8**, 2101266.
17. Y. Wu, J. Chen, J. Yuan, J. Xing, Z. Tan, L. Jiang, Q. Chen and J. Zhu, *J. Appl. Phys.*, 2016, **120**, 194103.
18. Z. Y. Shen, Z. Zhang, C. Qin, W. Luo, F. Song, Z. Wang and Y. Li, *J. Mater. Res.*, 2021, **36**, 1134-1141.
19. D. Wang, Y. Xu, Y. Shi, H. Wang, X. Wu, C. Wu, J. Zhu and Q. Chen, *J. Am. Ceram. Soc.*, 2019, **103**, 266-278.
20. Q. Xu, S. Xie, L. Li, J. Xing, Q. Chen, J. Zhu and Q. Wang, *J. Eur. Ceram. Soc.*, 2023, **43**, 916-927.
21. F. Zhang, W. Shi, S. Guan, Y. Xu, H. Yang, H. Chen, J. Xing, H. Liu and Q. Chen, *J. Alloys Compd.*, 2022, **907**, 164492.
22. N. Chen, F. Wang, X. Yang, H. Chen, Z. Tan, Q. Chen, J. Xing and J. Zhu, *J. Eur. Ceram.*

*Soc.*, 2024, **44**, 116788-116797.

23. N. Chen, F. Wang, X. Li, X. Yang, H. Chen, Z. Tan, J. Xing and J. Zhu, *Inorg. Chem.*, 2023, **62**, 6993-7002.
24. J. Xie, J. Zhong, C. Wu, Y. Shi, D. Wang, G. Liu, D. Liang, B. Wang, J. Zhu and Q. Chen, *J. Am. Ceram. Soc.*, 2018, **102**, 1287-1295.
25. X. Wu, W. Shi, S. Guan, S. Wang, Y. Cheng, L. Xie, H. Chen, Z. Tan, Y. Xu and Q. Chen, *J. Eur. Ceram. Soc.*, 2022, **42**, 119-128.
26. C. Long, W. Zhou, W. Ren, Y. Zhang, K. Zheng and L. Liu, *Scripta Mater.*, 2021, **204**, 114102-114108.
27. X. Wu, F. Zhang, X. Wang, H. Wang, Y. Chen, J. Zhu, Y. Xu, Y. Chen and Q. Chen, *J. Mater. Res.*, 2021, **36**, 1058-1066.
28. Z. Tan, J. Xi, J. Xing, B. Wu, Q. Zhang, Q. Chen and J. Zhu, *J. Eur. Ceram. Soc.*, 2022, **42**, 3865-3876.
29. J. Xi, J. Xing, J. Yuan, R. Nie, H. Chen, W. Zhang, Q. Chen and J. Zhu, *J. Mater. Sci-Mater. El.*, 2020, **31**, 8805-8814.
30. D. Jiang, Z. Zhou, R. Liang and X. Dong, *J. Eur. Ceram. Soc.*, 2021, **41**, 1244-1250.
31. W. Shi, S. Guan, X. Li, J. Xing, F. Zhang, N. Chen, Y. Wu, H. Xu, Y. Xu and Q. Chen, *J. Eur. Ceram. Soc.*, 2022, **42**, 6968-6976.
32. J. Xi, H. Chen, Z. Tan, J. Xing and J. Zhu, *Acta Mater.*, 2022, **237**, 118146.
33. F. Wang, X. Li, Q. Xu, H. Chen, J. Xi, F. Zhang, Z. Tan, Y. Cheng, S. Wang, J. Xing, Q. Chen and J. Zhu, *J. Eur. Ceram. Soc.*, 2022, **42**, 4196-4211.
34. X. Xie, Z. Zhou, R. Liang and X. Dong, *J. Materiomics*, 2021, **7**, 59-68.
35. X. Li, L. Zhu, P. Huang, Z. Chen, W. Bai, L. Li, F. Wen, P. Zheng, W. Wu, L. Zheng and Y. Zhang, *J. Appl. Phys.*, 2020, **127**, 044102.
36. X. Li, Z. Chen, L. Sheng, L. Li, W. Bai, F. Wen, P. Zheng, W. Wu, L. Zheng and Y. Zhang, *J. Eur. Ceram. Soc.*, 2019, **39**, 2050-2057.
37. L. Li, H. Yuan, P. Huang, Y. Zhang, L. Sheng, P. Zheng, L. Zhang, F. Wen, W. Wu and Z. Xu, *Ceram. Int.*, 2020, **46**, 2178-2184.
38. S. Jie, X. Jiang, C. Chen, X. Huang, X. Nie and H. Wang, *Ceram. Int.*, 2022, **48**, 6258-6265.
39. Z. Peng, Y. Chen, Q. Chen, N. Li, X. Zhao, C. Kou, D. Xiao and J. Zhu, *J. Alloys Compd.*, 2014, **590**, 210-214.
40. X. Xie, T. Wang, Z. Zhou, G. Cheng, R. Liang and X. Dong, *J. Eur. Ceram. Soc.*, 2019, **39**, 957-962.
41. W. Shi, Y. Wu, H. Tu, S. Guan, J. Xing, L. Xu, H. Xu and Q. Chen, *Scripta Mater.*, 2025, **258**, 116493.
42. J. Xu, S. Xie, Q. Xu, J. Xing, Q. Wang and J. Zhu, *J. Materiomics*, 2023, **10**, 652-669.
43. B. Zhang, S. Yu, Q. Li, Z. Luo, W. Li, M. Lin, J. Lang, M. Yuan, J. Deng, F. Yan, C. Long, D. Wang and L. Liu, *J. Eur. Ceram. Soc.*, 2025, **45**, 117101-117111.
44. B. Zhang, L. Quan, Z. Luo, Q. Li, J. Deng, S. Yu, W. Li, M. Lin, F. Yan, D. Wang, D. Yu, C. Long and L. Liu, *Mater. Today. Phys.*, 2024, **49**, 101598.
45. J. Zhong, C. Wu, D. Wang, Y. Shi, J. Zhu and Q. Chen, *J. Alloys Compd.*, 2019, **794**, 210-217.
46. A. Chen, Z. Chen, Y. Liu, P. Zheng, W. Bai, L. Li, F. Wen, L. Zheng and Y. Zhang, *Int. J.*

View Article Online
DOI: 10.1039/D5MH01252J

*Appl. Ceram. Tec.*, 2021, **18**, 2111-2120.

47. J. N. Chen, Q. Wang, X. Zhao and C. M. Wang, *J. Am. Ceram. Soc.*, 2022, **105**, 4815-4826.
48. C. Long, N. Ji, L. Yang, W. Zhou, K. Zheng, W. Ren and L. Liu, *J. Eur. Ceram. Soc.*, 2021, **41**, 3369-3378.
49. C. Long, B. Wang, W. Ren, K. Zheng, H. Fan, D. Wang and L. Liu, *Appl. Phys. Lett.*, 2020, **117**, 032902.
50. Q. Wang, E. M. Liang and C. M. Wang, *J. Am. Ceram. Soc.*, 2024, **107**, 7142-7152.
51. H. Wu, Z.-Y. Shen, Q. Wen, Z. Wang, T. Zeng, Z. Zhang, W. Luo and F. Song, *Ceram. Int.*, 2024, **50**, 50177-50184.
52. M. Tao, C. B. Pan, L. H. Yin, W. H. Song, X. B. Zhu, J. Yang and Y. P. Sun, *J. Mater. Sci-Mater. El.*, 2023, **34**, 535-546.
53. S. Guan, W. Shi, X. Wu and Q. Chen, *ACS Appl Mater Interfaces*, 2025, **17**, 36891-36898.
54. S. Guan, W. Shi, X. Wu, H. Xu, Y. Wu, R. Lang and Q. Chen, *J. Eur. Ceram. Soc.*, 2024, **44**, 2087-2094.
55. G. Kresse and J. Furthmu¨ller, *Phys. Rev. B*, 1996, **54**, 11169-11186.
56. J. P. Perdew, A. Ruzsinszky, G. I. Csonka, O. A. Vydrov, G. E. Scuseria, L. A. Constantin, X. Zhou and K. Burke, *Phys. Rev. Lett.*, 2008, **100**, 136406.
57. P. E. Blochl, *Phys. Rev. B Condens. Matter.*, 1994, **50**, 17953-17979.
58. X. Wu, D. Vanderbilt and D. R. Hamann, *Phys. Rev. B*, 2005, **72**, 035105.